


 Cite this: *RSC Adv.*, 2025, 15, 16219

Structural engineering of MXenes for enhanced magnesium ion diffusion: a computational study†

 Mingxiao Ma,[‡]^a Xiangyu Yao,[‡]^a Jianglong Wang,^a Xingqiang Shi,[Ⓜ]^a
 Ruining Wang,[Ⓜ]^a Ruqian Lian,[Ⓜ]^{*a} Dongxiao Kan^{*b} and Chenyang Jing^{*a}

The unique layered structure and tunable surface terminations of MXenes play a critical role in Mg²⁺ storage and diffusion dynamics. This study systematically investigates the behavior of Mg²⁺ in Ti₃C₂O₂ and its nitrogen-doped derivatives through theoretical calculations. In Ti₃C₂O₂ monolayers, Mg²⁺ exhibits a high diffusion barrier of 0.81 eV due to strong electrostatic interactions. However, AA-stacking reduces this barrier to 0.32 eV by introducing staggered active sites. The instability caused by interlayer O–O repulsion is mitigated by modulating the N/O ratio (Ti₃C₂O_{1.78}N_{0.22}), resulting in a diffusion barrier of 0.27 eV. Transition metal substitution further optimizes performance, as exemplified by Nb₃C₂N₂, which achieves an ultralow barrier of 0.23 eV through weakened N–N covalency and enhanced metal–N interactions. Voltage analysis reveals that Nb₃C₂N₂ possesses dual functionality as both cathode (4.00 V) and anode (0.64 V), contrasting with the anode-specific behavior observed in Ti-based MXenes.

 Received 21st March 2025
 Accepted 30th April 2025

DOI: 10.1039/d5ra01985k

rsc.li/rsc-advances

Introduction

With the rapid depletion of fossil fuels, sustainable energy storage solutions grow increasingly vital.¹ In the past few decades, rechargeable lithium-ion batteries (LIBs) have dominated portable electronics and energy storage systems through their high energy density and cycling stability.^{2,3} However, natural scarcity and dendritic growth risks of LIBs^{4–6} necessitate alternative solutions.⁷ Rechargeable magnesium ion batteries (MIBs) emerge as a promising alternative to LIB, offering high energy density and superior electrochemical stability.⁸ Mg is the fifth most abundant element in the Earth's crust,⁹ enabling substantial cost savings compared to Li. The melting temperature of Mg is measured at 923 K, much higher than that of Li (453.7 K), making MIBs the safer option for working at high temperatures like in aviation. Divalent Mg²⁺ delivers doubled volumetric capacity (3833 vs. 2046 mA h cm^{–3}) and dendrite-free operation with low reduction potential (–2.37 vs. SHE), and is expected to achieve reversible deposition in multiple electrolytes.^{8,10–12}

However, Mg²⁺ (0.72 Å) has a similar ionic radius to Li⁺ (0.76 Å).¹³ The large charge/radius ratio of Mg²⁺ leads to strong electrostatic interaction with the electrode framework, resulting in

sluggish ion diffusion.^{14,15} Previous research on MIB electrode materials mainly focused on the transition metal–oxygen/sulfide, polyanionic compounds, and other two-dimensional materials. In transition metal oxides/sulfides systems (*e.g.*, α-V₂O₅,¹⁶ α-MoO₃,¹⁷ Ti₂S₃/TiS₂ (ref. 18)), strong Mg²⁺–framework electrostatic interactions induce structural transformations that elevate Mg²⁺ diffusion barriers to 0.9–1.30 eV. By contrast, Chevrel phases and polyanionic compounds exhibit reversible Mg²⁺ (de)intercalation with mitigated electrostatic interactions.¹⁹ But even for polyanionic materials with good ion mobility, their energy barrier in MIBs is usually higher than 0.6 eV, such as Mg_{0.25}FePO₄ (1.03 eV) and NaV₂O₂(PO₄)₂F (0.78 eV).²⁰ Moreover, for the olivine-type Mg_xMnSiS₄, the strong Mn–S covalent interaction weakens the electrostatic interactions between Mg²⁺ and the host material ions, thereby enhancing Mg²⁺ diffusion compared to its oxide counterpart Mg_xMnSiO₄. However, the diffusion barrier for Mg²⁺ in Mg_xMnSiS₄ remains as high as 0.76 eV.

Transition metals-based layered materials have stable structures and excellent electrical conductivity.²¹ More importantly, the layered space provides a broad diffusion channel for Mg²⁺. Thus, 2D materials possess a lower diffusion barrier than the above materials, such as Si₂BN (0.08–0.35 eV), TiSe₂ (0.88 eV), VSe₂ (0.346 eV) and VS₂ (0.593 eV).^{22,23} As a layered material, MXenes have garnered significant attention in electrochemical energy storage due to their electrical conductivity, large specific surface area, and stable layered architecture for the guest ions.^{16,24,25} Lukatskaya *et al.* showed that Ti₃C₂T_x can provide ample accommodation to accommodate cations, such as Li⁺, Na⁺, K⁺, NH₄⁺, Mg²⁺ and Al³⁺, which produce large volumetric capacitance.²⁶ Xie *et al.*¹⁵ confirm that MXene monolayer cation

^aKey Laboratory of Optic-Electronic Information and Materials of Hebei Province, Hebei Research Center of the Basic Discipline for Computational Physics, College of Physics Science and Technology, Hebei University, Baoding 071002, China. E-mail: 16632719716@163.com; rqlian@126.com

^bNorthwest Institute for Non-ferrous Metal Research, Xi'an 710016, P. R. China. E-mail: kandx@c-nin.com

† Electronic supplementary information (ESI) available. See DOI: <https://doi.org/10.1039/d5ra01985k>

‡ Mingxiao Ma and Xiangyu Yao contributed equally to this work.



storage occurs in a comparatively low voltage window, which could be used as anodes for rechargeable batteries. Currently, about 40 MXenes have been synthesized experimentally and hundreds of new MXenes are simulated theoretically.^{27–30} It is crucial for MIB to investigate and enhance the diffusion performance of Mg ions within MXene materials.^{31,32} Moreover, traditional research on MXene batteries typically focuses on ion storage mechanisms under the default stacking configuration. In fact, the existence of different stacking types is an important feature of layered materials. The most typical example is the layered oxide cathode of potassium-ion batteries. Their different stacking structures can form different potassium-ion storage environments, such as edge-sharing octahedral (O3) or face-sharing prismatic (P2). O3-type materials have high structural stability and can effectively inhibit the migration of transition metals into the K layer, thereby reducing structural degradation during the cycling process. P2-type materials exhibit excellent rate performance due to their unique prismatic coordination environment, which provides shorter K ion migration paths and lower energy barriers. Obviously, stacking type has a significant impact on the storage and migration of ions.³³ However, research on the impact of stacking configurations on the MXene electrochemical properties and the corresponding modulation mechanisms is still lacking.

This work investigates the Mg²⁺ storage and diffusion mechanisms in MXene-based materials, emphasizing the interplay between structural configurations and electrochemical performance. Based on integrating stacking engineering, functional group modulation, and transition metal substitution strategies, we elucidate the fundamental principles governing Mg²⁺ behavior, such as mitigating electrostatic interactions, optimizing interlayer covalent bonding, and modulating electronic structures. These findings demonstrate that hierarchical structural design-stacking control, doping, and metal substitution-significantly enhances Mg²⁺ kinetics and stability, advancing high-performance MIB electrodes.

Method

All first-principles density functional theory (DFT) calculations are performed using the Vienna *Ab initio* Simulation Package (VASP)^{34–37} based on Perdew–Burke–Ernzerhof's (PBE) generalized gradient approximation (GGA-PBE).^{38,39} The plane wave truncation energy is set to 550 eV. The valence electron selection for pseudopotential elements is as follows: Mg-3s²3p⁰, O-2s²2p⁴, C-2s²2p², N-2s²2p³, Cl-3s²3p⁵, S-3s²3p⁴, F-2s²2p⁵, Ti-3d²4s², V-3d³4s², Zr-4d²5s², Nb-4d⁴5s¹. Considering the strong correlation system of transition metal D-orbital electrons, GGA + *U* method is adopted in the calculation, and the *U* values of Ti, Nb, V and Zr are set as 2.5 eV, 2.0 eV, 2.5 eV and 2.0 eV respectively, which are obtained from the reference of element *U* values given by Materials Studio software. Conjugate gradient method was used to optimize the lattice structure. The energy convergence standard was set to 10^{−6} eV per atom and the force convergence standard was set to 0.01 eV Å^{−1}. In addition, this work adopts the CI-NEB method^{40–42} to simulate the diffusion performance of Mg²⁺ in single/multilayer M₃C₂T_x (M = Ti, V, Zr, Nb, T = O, N)

in a 3 × 3 × 1 supercell model. Including the beginning and end positions before and after diffusion, a total of 7 insertion points are set, and the convergence standard is that the force of each insertion point is less than 0.03 eV Å^{−1}.

Results and discussion

Structure and properties of bulk phase Ti₃C₂O₂

The Ti₃C₂ structure is stacked by the Ti–C–Ti–C–Ti layer. In each layer, the atoms are arranged in hexagons. During the preparation of MXene, the –OH in the etched aqueous solution will spontaneously adsorb on the surface, forming –O terminated groups and water. Based on the type of molten salt and subsequent treatment conditions, other terminated groups, such as –Cl, –I, –Br, –S, –Se and –N could also be adsorbed on the surface of MXene layers. Among these function groups, previous theoretical studies mainly considered –O adsorbed in MXene electrode materials. Because divalent O^{2−} with a larger chemical activity has more affinity for the cation exposed framework. The adsorbed atoms inherit the hexagonal arrangement of the Ti–C–Ti–C–Ti layer, which distributes above the middle Ti atoms (Fig. 1).

Generally, the synthesized MXene materials are bulk rather than monolayer. According to the relative position of adjacent layers, the MXene structure has three possible stacking types, including AA (Table S1[†]), ABC₁ (Table S2[†]) and ABC₂ (Table S3[†]) types (Fig. 2a). For ABC₁ and ABC₂ types, terminal O is directly opposite to the outer Ti and C in the adjacent Ti₃C₂O₂ layer, respectively. The AA-stacking structure is characterized by the alignment of the terminal O groups of adjacent Ti₃C₂O₂ layers. According to the calculated phonon spectra, the phonon band for AA-stacking appears at −0.40 THz, which indicates a slight kinetic instability (Fig. 2b). By contrast, the phonon band structures without imaginary frequencies suggest that ABC₁ and ABC₂-stacking configurations are more likely to exist in nature. Moreover, our calculated relative energies show that the Ti₃C₂O₂ bulk with ABC₁-stacking is the most stable configuration (Fig. 2c). In comparison, the AA and ABC₂ types have relatively higher energy of 0.30 and 0.09 eV, respectively. Such relative stability of ABC₁-stacking is also applies consistently to the case of –Cl and –F terminate.

Adsorption of Mg²⁺ in Ti₃C₂O₂

Each surface of the Ti₃C₂O₂ layer has three possible Mg²⁺ active sites named H₁, H₂ and T, which are above the C, Ti and O atoms, respectively (Fig. 1a). H₁ and H₂ sites in two triangular hollow regions formed by three O and three Ti atoms, respectively. While the T site has only one coordinated O atom. To determine the most favorable Mg²⁺ active site, the Mg²⁺ binding energy *E_b* on the 2 × 2 × 1 Ti₃C₂O₂ monolayer was calculated through the following formula:

$$E_b = E_{\text{Ti}_3\text{C}_2\text{N}_2\text{Mg}_x} - E_{\text{Ti}_3\text{C}_2\text{N}_2} - xE_{\text{Mg}} \quad (1)$$

where *E_{Mg,Ti₃C₂O₂}*, *E_{Ti₃C₂O₂}* and *E_{Mg}* are the total energy of Ti₃C₂O₂Mg_x, Ti₃C₂O₂ and one atom of metal Mg. The calculation results show that the H₁ site exhibited a more negative *E_b* (−2.16 eV) than H₂ (−1.36 eV) site. While the Mg²⁺ on T site migrates to



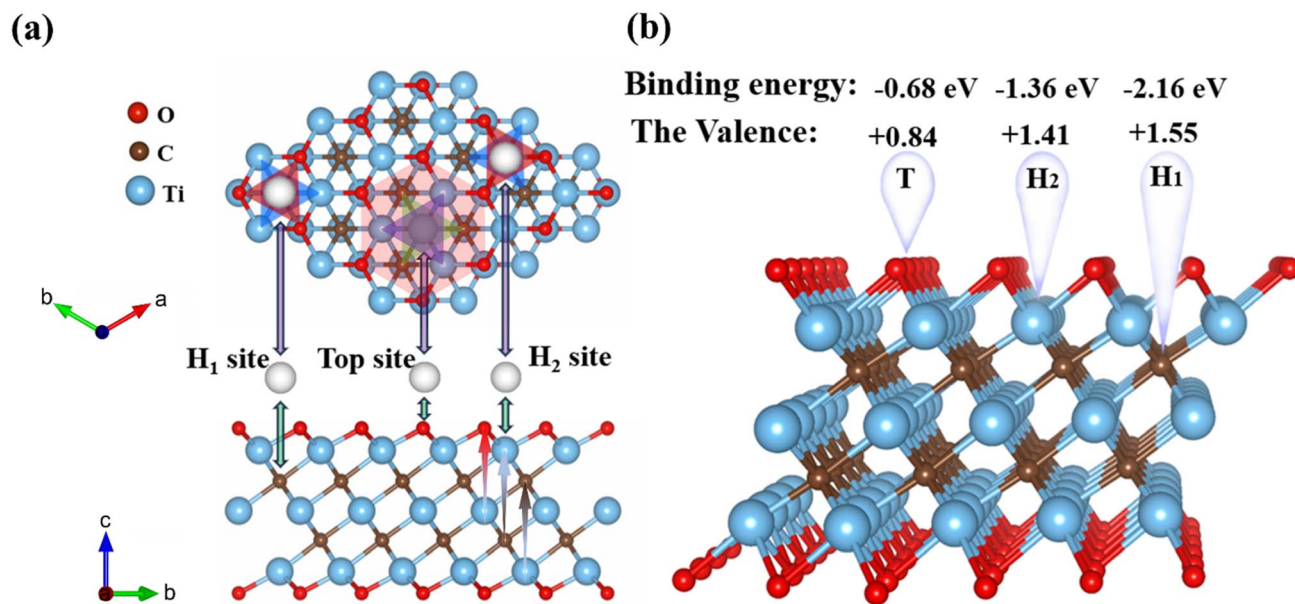


Fig. 1 (a) The top and side views of the three Mg^{2+} adsorption sites, namely, H_1 , H_2 and T site on monolayer $Ti_3C_2O_2$. (b) Binding energy and valence states of Mg^{2+} at H_1 , H_2 and T sites.

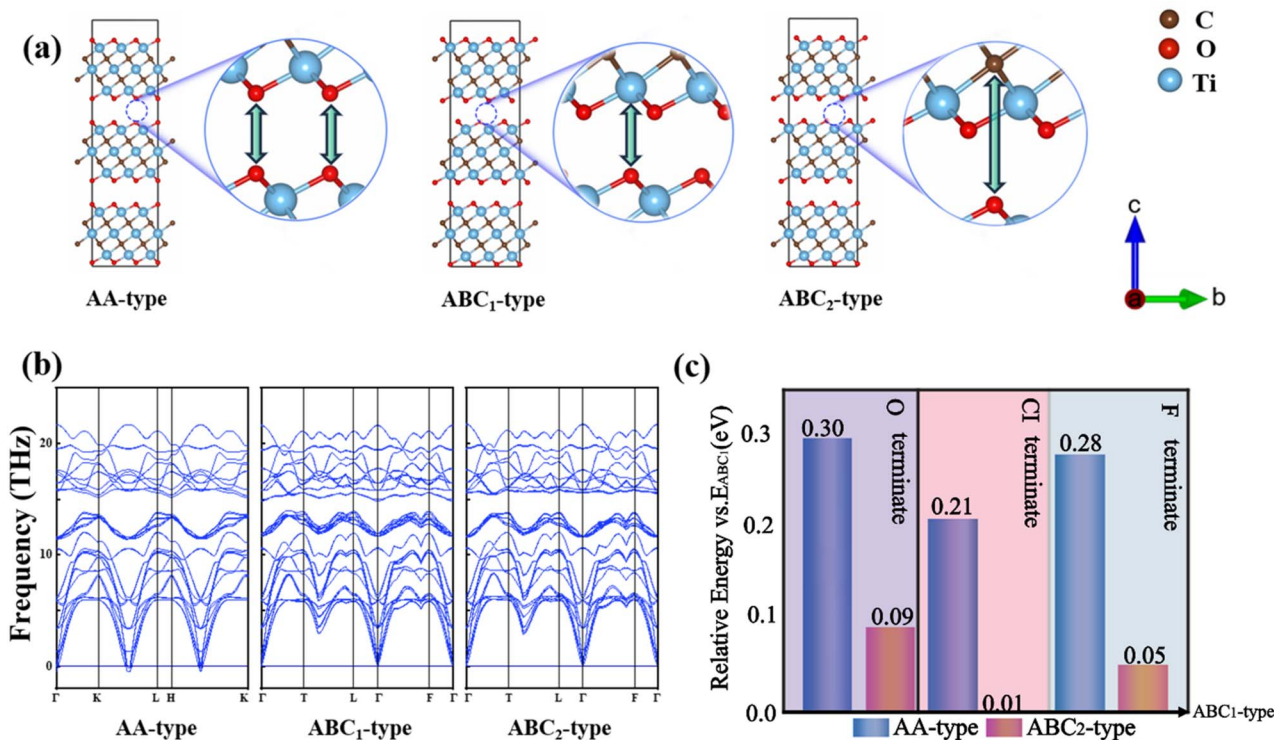


Fig. 2 (a) The side-views of the three stacked $Ti_3C_2O_2$, namely ABC_1 type, AA type and ABC_2 type. (b) The phonon band structures of AA-, ABC_1 - and ABC_2 -stacked configuration. (c) The relative energy of ABC_1 - and ABC_2 -type vs. the energy of AA-type for $Ti_3C_2O_2$, $Ti_3C_2Cl_2$ and $Ti_3C_2F_2$, respectively, in left to right order.

the adjacent H_1 site after structural optimization. In the case of fixed Mg^{2+} at a specific xy coordinate, the binding energy at the T site is only -0.68 eV. This indicates that a low coordination degree is not favorable for Mg^{2+} storage. According to the Bader charge analysis, the valence states of Mg^{2+} on H_1 , H_2 and T site

was $+1.55$, $+1.41$ and $+0.84$, respectively (Fig. 1b). Obviously, Mg^{2+} at the H_1 site is closer to its theoretical standard valence state, which is more conducive to its binding. When the $Ti_3C_2O_2$ layers are stacked to form the bulk, the Mg^{2+} active site is provided by both upper and lower $Ti_3C_2O_2$ layers. All possible



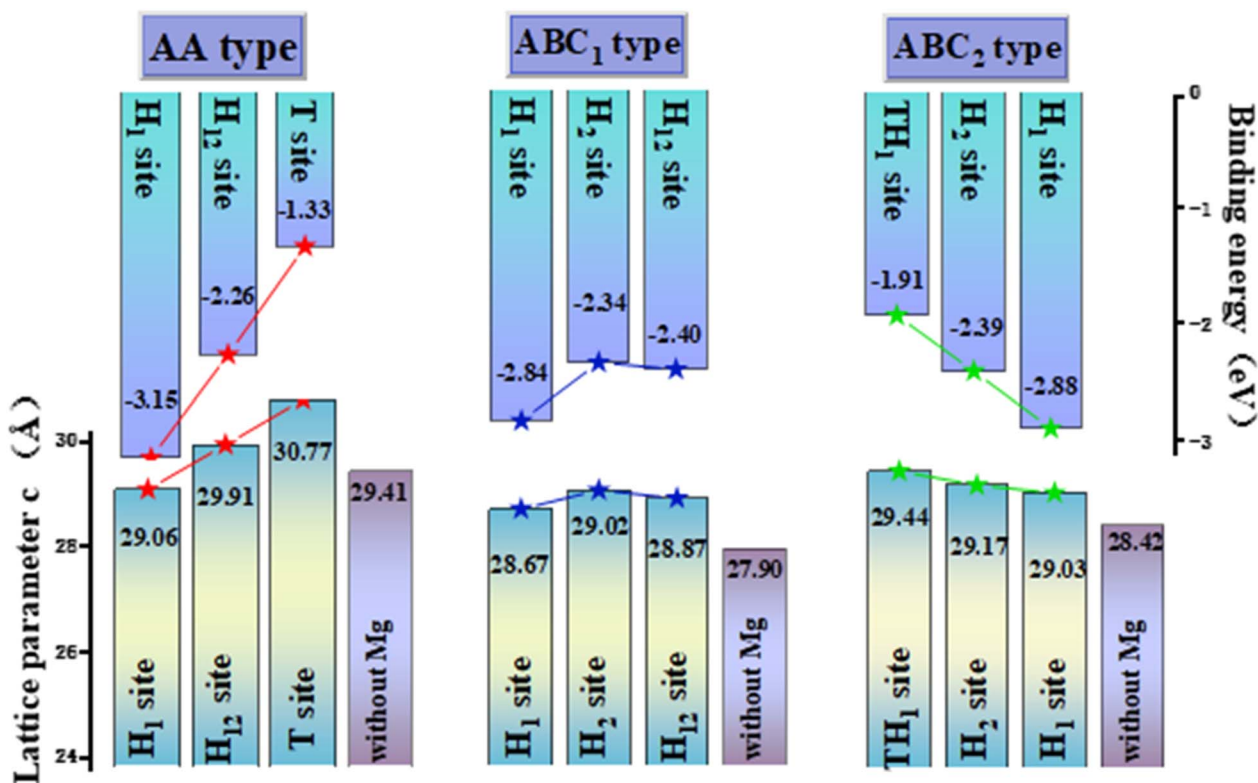


Fig. 3 The binding energy of Mg^{2+} at each adsorption site of $\text{Ti}_3\text{C}_2\text{O}_2$ and the change trend of lattice parameter c .

adsorption sites of Mg^{2+} in the three 42 configurations are taken into account. For the AA-stacking type, the two $\text{Ti}_3\text{C}_2\text{O}_2$ layers form H_1 , H_{12} and T active sites for Mg^{2+} , where the “ H_{12} ” site means the combination of the H_1 and H_2 sites from two adjacent $\text{Ti}_3\text{C}_2\text{O}_2$ layers, respectively. ABC_1 - $\text{Ti}_3\text{C}_2\text{O}_2$ forms H_1 , H_2 and H_{12} sites. ABC_2 - $\text{Ti}_3\text{C}_2\text{O}_2$ forms TH_1 , H_1 and H_2 sites. For all these three stacking configurations, the H_1 site exhibited stronger binding energy than the other sites (Fig. 3), which is consistent with the Mg^{2+} adsorption behavior for $\text{Ti}_3\text{C}_2\text{O}_2$ monolayer. Among the three configurations, the H_1 site in AA-stacked structure exhibited the most negative adsorption energy, which indicated that the AA-stacking is more favorable adsorptive configuration for Mg^{2+} . According to the optimized crystal, the lower the binding energy, the smaller the lattice parameter c . This suggests that the strong coulomb attraction between the O atoms and the adsorbed Mg^{2+} can mitigate volume expansion during ion storage. Moreover, it is evident that the structural energy difference between the ABC_1 - and ABC_2 - $\text{Ti}_3\text{C}_2\text{O}_2$ is very small (Fig. 2c and 4). Furthermore, during structural optimized, Mg^{2+} adsorbed ABC_2 - $\text{Ti}_3\text{C}_2\text{O}_2$ will relax into ABC_1 type through the sliding of adjacent $\text{Ti}_3\text{C}_2\text{O}_2$ layers. Therefore, the ABC_2 configuration is improbable to form under practical conditions and will hence not be considered in subsequent studies.

Mg^{2+} diffuses in AA, ABC_1 and monolayer $\text{Ti}_3\text{C}_2\text{O}_2$

The rate performance of anode is determined by the kinetics of electronic and ionic diffusion. To further study the Mg^{2+}

diffusion kinetic properties for the AA- and ABC_1 -stacking structures, the Mg^{2+} diffusion barrier is evaluated in the $3 \times 3 \times 1$ $\text{Ti}_3\text{C}_2\text{O}_2$ bulk/monolayer using the CI-NEB method. In each configuration, Mg^{2+} is simulated to migrate between two energetically favorable active sites (Fig. 4a). On $\text{Ti}_3\text{C}_2\text{O}_2$ monolayer, the diffusion of Mg^{2+} between two adjacent H_1 sites across H_2 site (described as $\text{H}_1 \rightarrow \text{H}_2 \rightarrow \text{H}_1$) has a relatively large barrier of 0.81 eV (Fig. 4d). Such a value is close to the Mg^{2+} barrier (0.72 eV) on the Ti_2NO_2 monolayer reported by Wang *et al.*²⁸ According to that work, the univalent Li^+ , Na^+ , K^+ diffusion barriers are lower than 0.3 eV, which suggests that the pathway of Ti_2NO_2 monolayer is insufficient to provide an adequate coordination environment for the bivalent Mg^{2+} .

In the AA-stacking $\text{Ti}_3\text{C}_2\text{O}_2$, the Mg^{2+} barrier is significantly improved to 0.32 eV. The optimized AA-stacking structure shows that the adjacent H_{12} active sites provided by the upper and lower $\text{Ti}_3\text{C}_2\text{O}_2$ surfaces are opposite, which can be described as “ $\text{H}_2 \rightarrow \text{H}_1 \rightarrow \text{H}_2$ ” (Fig. 4b). Notably, compared with the $\text{Ti}_3\text{C}_2\text{O}_2$ monolayer, Mg^{2+} can only move from $\text{H}_2 \rightarrow \text{H}_1$ through a single step, and can thereby transfer from $\text{H}_1 \rightarrow \text{H}_2$ on one H_1 active site to another. It can be seen that the periodic migration path of Mg^{2+} has been shortened by almost half. Besides, according to the CI-NEB method, the ionic migration barrier is obtained by subtracting the energy of the stable state (SS) from that of the transition state (TS), *i.e.*, $E_{\text{barrier}} = E_{\text{TS}} - E_{\text{SS}}$.⁴³ The contribution of metastable H_2 site in AA- $\text{Ti}_3\text{C}_2\text{O}_2$ increases the E_{SS} , alleviating energy changes during Mg^{2+}



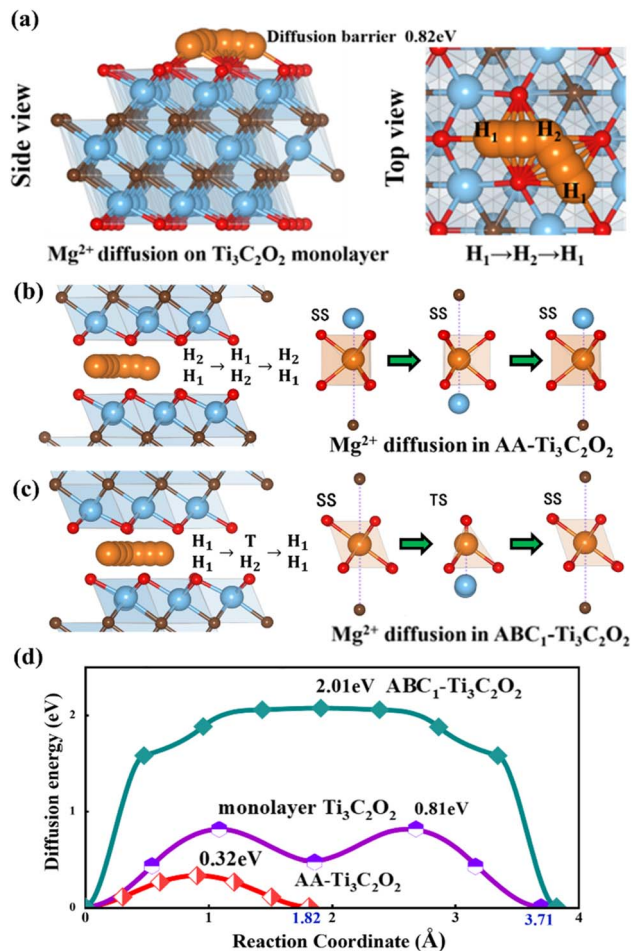


Fig. 4 (a) Diffusion path of magnesium on single layer $\text{Ti}_3\text{C}_2\text{O}_2$ surface. (b) Diffusion paths of Mg^{2+} in AA type and (c) ABC_1 type $\text{Ti}_3\text{C}_2\text{O}_2$ structure, respectively. (d) Diffusion energy barrier of Mg^{2+} in AA type, ABC_1 type and single layer $\text{Ti}_3\text{C}_2\text{O}_2$.

migration. In comparison, the Mg^{2+} diffusion channel in the $\text{ABC}_1\text{-Ti}_3\text{C}_2\text{O}_2$ can be described as " $\text{H}_1 \rightarrow \text{T} \rightarrow \text{H}_1$ " (Fig. 4c). The stable active site composed of two stable H_1 sites lead to a low E_{SS} value. While the metastable H_2 and exceptionally unstable T site significantly increases the E_{TS} . Such substantial energy disparity between E_{TS} and E_{SS} lead to a large diffusion barrier of 2.01 eV for $\text{ABC}_1\text{-Ti}_3\text{C}_2\text{O}_2$. To further investigate the influencing factors of Mg^{2+} diffusion barrier, the Bader charge of Mg^{2+} in stable states (e_{S}) and transition states (e_{T}) as well as the charge difference ($\Delta e = |e_{\text{S}} - e_{\text{T}}|$) between them were calculated based on the CI-NEB image. The result showed that the Δe for AA and ABC_1 types are 0.005 and 0.206e, which are consistent with their barrier order of 0.32, and 2.01 eV, respectively. The Mg^{2+} channel in $\text{ABC}_1\text{-Ti}_3\text{C}_2\text{O}_2$ has large fluctuation on electron capture, which is also an important factors that cause the largest diffusion barrier.

Diffusion of Mg^{2+} in $\text{AA-Ti}_3\text{C}_2\text{T}_x$ ($\text{T} = \text{O}, \text{N}$)

According to the above discussion, the adsorption and migration behavior of Mg^{2+} exhibits a pronounced preference for the

AA- $\text{Ti}_3\text{C}_2\text{O}_2$. Regrettably, in layered stacking structures, the coulombic effect between layers significantly influence the stacking configuration. For the AA- $\text{Ti}_3\text{C}_2\text{O}_2$, the O-O electrostatic repulsion from the adjacent layers leads to a preference for staggered arrangement in $\text{Ti}_3\text{C}_2\text{O}_2$ bulk, thereby increasing the interlayer spacing and rendering the AA- $\text{Ti}_3\text{C}_2\text{O}_2$ unstable. One effective approach to mitigate electrostatic repulsion is to substitute bivalent O with monovalent halogens such as F or Cl. However, the introduction of F/Cl functional groups does reduce the energy difference between the AA- and $\text{ABC}_1\text{-Ti}_3\text{C}_2\text{O}_2$, yet the AA configuration remains relatively unstable (Fig. 2c). The remaining stacking control method is to utilize higher valence N as functional group, thereby converting electrostatic repulsion into covalent bonding through the addition of electrons.

Consequently, the O function group in AA, ABC_1 and ABC_2 configurations are replaced by N (Fig. 5a). The calculated relative energy revealed that the AA-type $\text{Ti}_3\text{C}_2\text{N}_2$ become the most stable configuration. Taking AA- $\text{Ti}_3\text{C}_2\text{N}_2$ as the reference structure, the relative energies of ABC_1 and ABC_2 are 6.82 eV and 7.89 eV, respectively (Fig. 5b). Such large values indicate that the introduction of interlayer N-N covalent bonding significantly enhances the stability of the AA-stacking configuration. In the AA- $\text{Ti}_3\text{C}_2\text{N}_2$ system, the diffusion energy barrier of Mg^{2+} calculated using the CI-NEB method is 1.07 eV, which is 0.94 eV lower than that in the stable ABC_1 configuration for $\text{Ti}_3\text{C}_2\text{O}_2$. Evidently, the electrostatic interaction between layers does not directly influence the migration of Mg^{2+} . Instead, it indirectly facilitates a favorable migration environment for Mg^{2+} by inducing structural changes. Despite this reduction, the barrier of 1.07 eV still represents a poor diffusion performance. This can be attributed to the strong bonding between nitrogen atoms in adjacent $\text{Ti}_3\text{C}_2\text{N}_2$ layers, which results in reduced layer spacing and hinders the migration of Mg^{2+} . Consequently, it is crucial to determine an appropriate N doping concentration to maintain optimal layer spacing while controlling the MXene stacking type.

The calculation of the relative energies for AA and ABC_1 configurations with varying N contents reveals that when the N

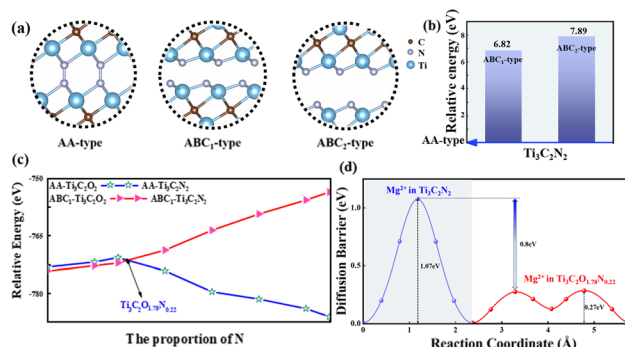


Fig. 5 (a) AA-, ABC_1 - and ABC_2 - $\text{Ti}_3\text{C}_2\text{N}_2$ interlayer structure. (b) The relative energy of ABC_1 - and ABC_2 - $\text{Ti}_3\text{C}_2\text{N}_2$ with respect to AA-type. (c) The relative energies of AA and ABC_1 configurations with different N content. (d) Diffusion barrier comparison of Mg^{2+} in AA-stacking $\text{Ti}_3\text{C}_2\text{N}_2$ and $\text{Ti}_3\text{C}_2\text{N}_{1.78}\text{N}_{0.22}$ structures.



concentration reaches 11%, the stable phase MXene bulk transitions to the AA-stacking type, corresponding to the chemical formula $\text{Ti}_3\text{C}_2\text{O}_{1.78}\text{N}_{0.22}$ (Fig. 5c). For this configuration, the Mg^{2+} diffusion barrier is decreased to 0.27 eV, which is significantly lower by 0.8 eV compared to $\text{Ti}_3\text{C}_2\text{N}_2$ bulk. Notably, Mg^{2+} diffusion predominantly occurs near O functional groups rather than N functional groups (Fig. 5d). This can be attributed to the additional energy required for Mg^{2+} to overcome the interlayer N–N covalent bonds during diffusion, thereby increasing the migration energy barrier.

On the other hand, the strong interlayer N–N covalent bonding in the AA- $\text{Ti}_3\text{C}_2\text{N}_2$ structure is primarily responsible for the poor Mg diffusion kinetic property. Based on the such bonding situation, it can be proposed that enhancing the metal–N bond strength may weaken the interlayer N–N covalency, thereby improving ionic conductivity. In the periodic table, we have selected three transition metal elements, V, Zr and Nb, to substitute for Ti in AA- $\text{Ti}_3\text{C}_2\text{N}_2$. V ($3d^34s^2$), Nb ($4d^45s^1$), and Zr ($4d^25s^2$) each enhance N bonding through distinct mechanisms compared to Ti ($3d^24s^2$). V and Nb provide additional valence electrons for covalent interactions, while Zr achieves stronger binding *via* reduced electronegativity-driven ionic attraction. After replacing Ti atoms in AA-stacking $\text{Ti}_3\text{C}_2\text{N}_2$ with V, Zr and Nb, the dynamical stability of these four conformations are checked through examining the phonon band structures (Fig. 6a–d), which indicated that they are dynamically stable configurations with no states associated with imaginary frequencies.

Diffusion of Mg^{2+} in AA- $\text{M}_3\text{C}_2\text{N}_2$ ($\text{M} = \text{Nb}, \text{V}, \text{Zr}$)

Subsequently, to analyze the diffusion behavior of Mg^{2+} in AA- $\text{M}_3\text{C}_2\text{N}_2$ ($\text{M} = \text{V}, \text{Zr}$ and Nb), the Mg^{2+} migration pathways and corresponding energy barriers are investigated within $3 \times 3 \times 1$ supercell. With a single Mg^{2+} intercalation into $\text{M}_3\text{C}_2\text{N}_2$, it was relaxed to the H_2 site after structure optimization and the corresponding the half of diffusion pathways were described as $\text{H}_2 \rightarrow \text{H}_1$, which showed that Mg^{2+} diffusion behavior in $\text{M}_3\text{C}_2\text{N}_2$ bulks (including $\text{Ti}_3\text{C}_2\text{N}_2$) is consistent. The diffusion barriers of Mg^{2+} in $\text{V}_3\text{C}_2\text{N}_2$, $\text{Zr}_3\text{C}_2\text{N}_2$ and $\text{Nb}_3\text{C}_2\text{N}_2$ had decreased compared with in $\text{Ti}_3\text{C}_2\text{N}_2$ by 0.37 eV, 0.79 eV and 0.84 eV, respectively. Notably, $\text{Nb}_3\text{C}_2\text{N}_2$ exhibits the smallest barrier of 0.23 eV. This indicates that N–N covalent binding is weakened more effectively by replacing Ti with Nb than with V and Zr (Fig. 6e). Overall, the $\text{Nb}_3\text{C}_2\text{N}_2$ obtained by using the transition metal element Nb to replace Ti in AA- $\text{Ti}_3\text{C}_2\text{N}_2$ has the lowest energy barrier (Fig. S1†).

Theoretical voltage value of AA-stacking $\text{Nb}_3\text{C}_2\text{N}_2$

According to the above discussion, the favorite absorption site of Mg^{2+} is H_2 site. Based on this, the formation energy of $\text{Nb}_3\text{C}_2\text{N}_2\text{Mg}_x$ ($0 \leq x \leq 1$) was calculated *via* the following equation to explore the thermodynamically stable Mg-containing phases,

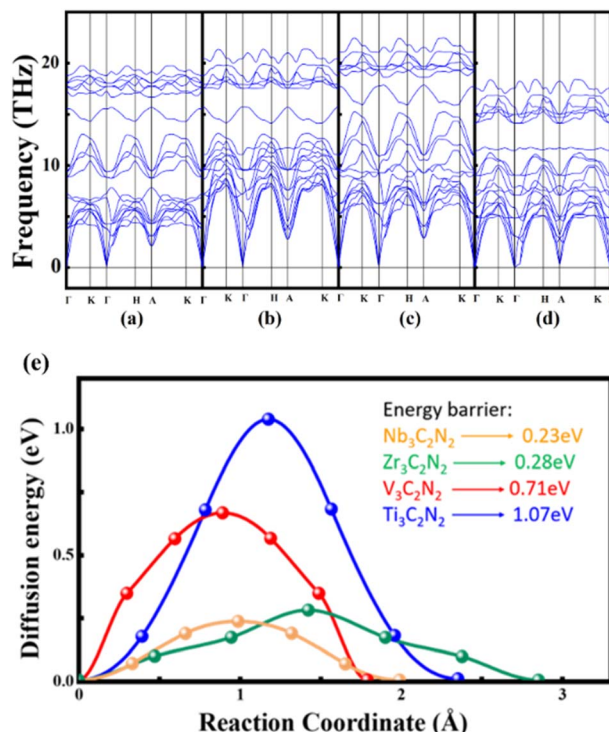


Fig. 6 Phonon spectra of (a) $\text{Nb}_3\text{C}_2\text{N}_2$, (b) $\text{Ti}_3\text{C}_2\text{N}_2$, (c) $\text{V}_3\text{C}_2\text{N}_2$ and (d) $\text{Zr}_3\text{C}_2\text{N}_2$. (e) Diffusion energy barrier of Mg^{2+} in AA- $\text{M}_3\text{C}_2\text{N}_2$ ($\text{M} = \text{Ti}, \text{V}, \text{Zr}, \text{Nb}$).

$$E_f = E_{\text{Nb}_3\text{C}_2\text{N}_2\text{Mg}_x} - \left(1 - \frac{x}{2}\right)E_{\text{Nb}_3\text{C}_2\text{N}_2} - \frac{x}{2}E_{\text{Nb}_3\text{C}_2\text{N}_2\text{Mg}_2} \quad (2)$$

where $E_{\text{Nb}_3\text{C}_2\text{N}_2\text{Mg}_x}$, $E_{\text{Nb}_3\text{C}_2\text{N}_2\text{Mg}_2}$ and $E_{\text{Nb}_3\text{C}_2\text{N}_2}$ are total energies for $\text{Nb}_3\text{C}_2\text{N}_2\text{Mg}_x$, $\text{Nb}_3\text{C}_2\text{N}_2\text{Mg}_2$ and $\text{Nb}_3\text{C}_2\text{N}_2$, correspondingly, x is the Mg^{2+} adsorption degrees in $\text{Nb}_3\text{C}_2\text{N}_2\text{Mg}_x$, including 0, 0.25, 0.5, 0.75, 1, 1.25, 1.5, 1.75 and 2 (Fig. 7a). Our result suggests that the thermodynamically stable configurations are $\text{Nb}_3\text{C}_2\text{N}_2\text{Mg}_{0.75}$, $\text{Nb}_3\text{C}_2\text{N}_2\text{Mg}$ and $\text{Nb}_3\text{C}_2\text{N}_2\text{Mg}_2$, with their E_f points located at the bottom edge of the convex hull. Based on this, the open circuit voltage (OCV) of AA-stacking $\text{Nb}_3\text{C}_2\text{N}_2$ with different Mg^{2+} adsorption degrees is calculated from the following formula,

$$V = \frac{1}{n} \left| \frac{2(E_{\text{Nb}_3\text{C}_2\text{N}_2\text{Mg}_{x_2}} - E_{\text{Nb}_3\text{C}_2\text{N}_2\text{Mg}_{x_1}})}{(x_2 - x_1)} - E_{\text{Mg}} \right| \quad (3)$$

where $E_{\text{Nb}_3\text{C}_2\text{N}_2\text{Mg}_{x_2}}$ and $E_{\text{Nb}_3\text{C}_2\text{N}_2\text{Mg}_{x_1}}$ are the total energies of $\text{Nb}_3\text{C}_2\text{N}_2$ with different Mg^{2+} adsorption degrees x_1 and x_2 , E_{Mg} is the energy of a Mg atom in metal Mg, charge value $n = 2$ for Mg^{2+} . Interestingly, the calculated voltages contain two distinct plateaus at 4.00 V and 0.64 V, corresponding to the ranges of $x = 0-0.75$ and $x = 1-2$, respectively (Fig. 7b). This results indicate that when a monolayer of Mg^{2+} is intercalated between the $\text{Nb}_3\text{C}_2\text{N}_2$ layers, the binding affinity of Mg^{2+} to the $\text{Nb}_3\text{C}_2\text{N}_2$ layers significantly decreases. Such a significant voltage difference indicates that the material can function as both the positive and negative electrode of the battery under varying ion concentrations. This behavior is analogous to that observed in



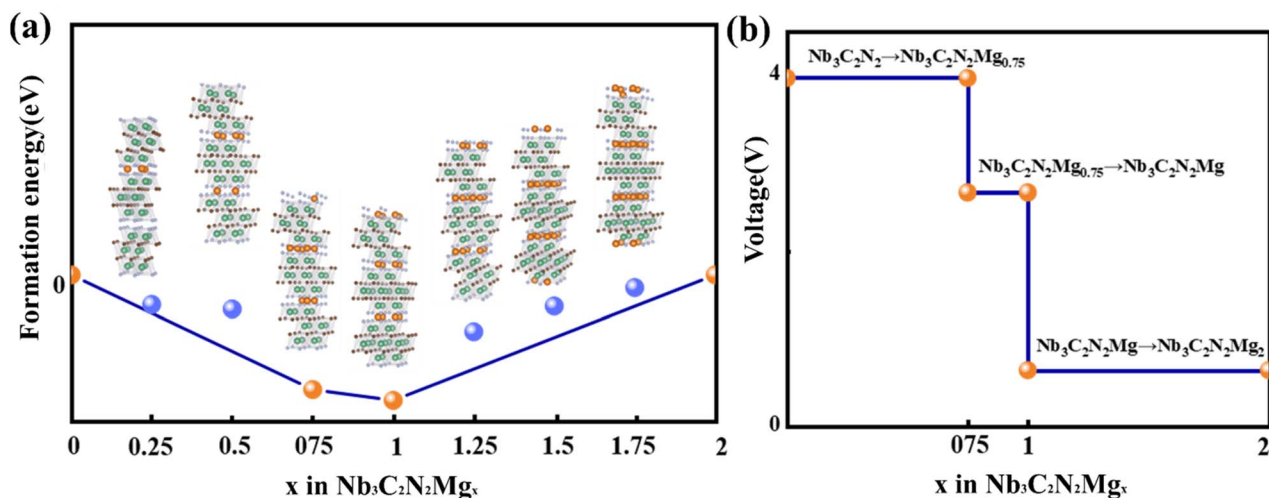


Fig. 7 (a) Formation energy and (b) theoretical voltage value of $\text{Nb}_3\text{C}_2\text{N}_2\text{Mg}_x$.

Prussian blue materials used in potassium-ion batteries.⁴⁴ By contrast, the voltage platforms presented by Ti-based MXene belong to the anode range (Fig. S2†). From a voltage stability perspective, $\text{Ti}_3\text{C}_2\text{O}_2\text{Mg}_x$ and $\text{Ti}_3\text{C}_2\text{O}_{1.78}\text{N}_{0.22}\text{Mg}_x$ exhibit three short platforms decreasing in the concentration of $0 < x < 1$. Although $\text{Ti}_3\text{C}_2\text{N}_2$ possesses two stable platforms, the voltage of 0.02 V is too low for electrode, which is easy to transform the Mg^{2+} intercalation mechanism into electroplating.

Conclusions

This study systematically investigates the Mg^{2+} storage and diffusion mechanisms in MXene materials, focusing on $\text{Ti}_3\text{C}_2\text{O}_2$ and its nitrogen-doped derivatives. The strong electrostatic interaction between divalent Mg^{2+} and electrode frameworks leads to high diffusion barriers (0.81 eV in monolayers), which are mitigated by optimizing MXene stacking configurations and functional group engineering. AA-stacking $\text{Ti}_3\text{C}_2\text{O}_2$ exhibits strong Mg^{2+} adsorption energy of -2.16 eV and low diffusion barrier of 0.32 eV due to staggered active sites shortening migration paths. However, its instability from interlayer O–O repulsion necessitates structural modifications. Replacing O with N transforms stable $\text{ABC}_1\text{-Ti}_3\text{C}_2\text{O}_2$ to $\text{AA-Ti}_3\text{C}_2\text{N}_2$ through enhanced interlayer N–N covalent bonding. However, excessive N doping increases the energy barrier (1.07 eV) due to decreased layer spacing. One effective approach is to control the N/O ratio, which balances interlayer spacing and covalent interactions, resulting in an energy barrier of 0.27 eV in the $\text{Ti}_3\text{C}_2\text{O}_{1.78}\text{N}_{0.22}$ structure. Another strategy involves substituting transition metals into the MXene framework to modulate interlayer bonding. Introducing transition metals (V, Zr, Nb) into $\text{Ti}_3\text{C}_2\text{N}_2$ weakens N–N covalency, with $\text{Nb}_3\text{C}_2\text{N}_2$ achieving an ultralow barrier of 0.23 eV. $\text{Nb}_3\text{C}_2\text{N}_2$ possesses dual voltage platforms (4.00 V and 0.64 V), enabling its dual role as cathode/anode, while Ti-based MXenes exhibit anode-specific behavior. These findings highlight that tailored MXene structures, through stacking control, nitrogen doping, and metal substitution, significantly enhance Mg^{2+} kinetics and stability,

positioning them as promising high-performance electrodes for next-generation Mg-ion batteries.

Data availability

The datasets used and/or analyzed during the current study are available from the corresponding author upon reasonable request.

Conflicts of interest

There are no conflicts to declare.

Acknowledgements

This work was supported by the Hebei Natural Science Foundation Youth Foundation (No. 606020324086), the Advanced Talents Incubation Program of the Hebei University (No. 521000981394), the Scientific Research and Innovation Team of Hebei University (Grant No. IT2023B03) and the High-Performance Computing Center of Hebei University.

References

- 1 Y. Shabeer, S. S. Madani, S. Panchal, M. Mousavi and M. Fowler, Different Metal–Air Batteries as Range Extenders for the Electric Vehicle Market: A Comparative Study, *Batteries*, 2025, **11**(1), 35.
- 2 D. A. Kolosov and O. E. Glukhova, High-Capacity Ion Batteries Based on Ti_2C MXene and Borophene First Principles Calculations, *Inorganics*, 2023, **11**(3), 95.
- 3 X. Zhang, A. Wang, X. Liu and J. Luo, Dendrites in Lithium Metal Anodes: Suppression, Regulation, and Elimination, *Acc. Chem. Res.*, 2019, **52**(11), 3223–3232.
- 4 F. Sun, H. Liu, L. Ni and X. Wang, Growth Mechanisms of Li Dendrite and the Suppression Strategies, *Chin. Sci. Bull.*, 2021, **66**(9), 1046–1056.



- 5 X. Chen, B. Zhao, C. Yan and Q. Zhang, Review on Li Deposition in Working Batteries: From Nucleation to Early Growth, *Adv. Mater.*, 2021, **33**(8), 2004128.
- 6 Y.-G. Lee, S. Fujiki, C. Jung, N. Suzuki, N. Yashiro, R. Omoda, D.-S. Ko, T. Shiratsuchi, T. Sugimoto, S. Ryu, J. H. Ku, T. Watanabe, Y. Park, Y. Aihara, D. Im and I. T. Han, High-Energy Long-Cycling All-Solid-State Lithium Metal Batteries Enabled by Silver–Carbon Composite Anodes, *Nat. Energy*, 2020, **5**(4), 299–308.
- 7 G. A. Shaikh, A. M. Satawara, S. K. Gupta and P. N. Gajjar, Unlocking the Potential of Mg-Ion Batteries: Cu₂C MXene Anode with Ultrahigh Storage and Energy Density with Rapid Mg Diffusion, *Chem. Eng. J.*, 2024, **498**, 155368.
- 8 R. Dominko, J. Bitenc, R. Berthelot, M. Gauthier, G. Pagot and V. Di Noto, Magnesium Batteries: Current Picture and Missing Pieces of the Puzzle, *J. Power Sources*, 2020, **478**, 229027.
- 9 Y. Du, Y. Chen, S. Tan, J. Chen, X. Huang, L. Cui, J. Long, Z. Wang, X. Yao, B. Shang, G. Huang, X. Zhou, L. Li, J. Wang and F. Pan, Strong Solvent Coordination Effect Inducing Gradient Solid-Electrolyte-Interphase Formation for Highly Efficient Mg Plating/Stripping, *Energy Storage Mater.*, 2023, **62**, 102939.
- 10 K. A. Papadopoulou, A. Chroneos and S.-R. G. Christopoulos, Mg-Ion Diffusion on the Surface of Ti₃C₂S₂ MXene, *J. Phys. Chem. Solids*, 2022, **166**, 110713.
- 11 B. Li, R. Masse, C. Liu, Y. Hu, W. Li, G. Zhang and G. Cao, Kinetic Surface Control for Improved Magnesium-Electrolyte Interfaces for Magnesium Ion Batteries, *Energy Storage Mater.*, 2019, **22**, 96–104.
- 12 M. Deng, L. Wang, B. Vaghefnazari, W. Xu, C. Feiler, S. V. Lamaka, D. Höche, M. L. Zheludkevich and D. Snihirova, High-Energy and Durable Aqueous Magnesium Batteries: Recent Advances and Perspectives, *Energy Storage Mater.*, 2021, **43**, 238–247.
- 13 J. Nai, Y. Han, S. Zhang, Y. Li, X. Chen, R. Wu, L. Wang and L. Jiang, Sulfite Activation by ZnO-Encapsulated Hydrogels for Degradation of Trimethylphenol, *Nano Res.*, 2023, **16**(10), 12345–12356.
- 14 M. Hammouri, M. Arsentev and A. Petrov, Ab Initio Studies of Ti₂S₃ as a New Cathode Material for Magnesium Secondary Batteries, *Mater. Today Commun.*, 2019, **20**, 100598.
- 15 Y. Xie, Y. Dall'Agnese, M. Naguib, Y. Gogotsi, M. W. Barsoum, H. L. Zhuang and P. R. C. Kent, Prediction and Characterization of MXene Nanosheet Anodes for Non-Lithium-Ion Batteries, *ACS Nano*, 2014, **8**(9), 9606–9615.
- 16 R. Xiao, J. Xie, T. Luo, L. Huang, Y. Zhou, D. Yu, C. Chen and Y. Liu, Phase Transformation and Diffusion Kinetics of V₂O₅ Electrode in Rechargeable Li and Mg Batteries: A First-Principle Study, *J. Phys. Chem. C*, 2018, **122**(3), 1513–1521.
- 17 T. A. Barnes, L. F. Wan, P. R. C. Kent and D. Prendergast, Hybrid DFT Investigation of the Energetics of Mg Ion Diffusion in α -MoO₃, *Phys. Chem. Chem. Phys.*, 2018, **20**(38), 24877–24884.
- 18 D. S. Tchitchekova, A. Ponrouch, R. Verrelli, T. Broux, C. Frontera, A. Sorrentino, F. Bardé, N. Biskup, M. E. Arroyo-de Dompablo and M. R. Palacín, Electrochemical Intercalation of Calcium and Magnesium in TiS₂: Fundamental Studies Related to Multivalent Battery Applications, *Chem. Mater.*, 2018, **30**(3), 847–856.
- 19 G. Li, Z. Yao and C. Li, In-Situ Multi-Scale Structural Engineering of Cathode and Electrolyte for High-Rate and Long-Life Mg Metal Batteries, *J. Energy Chem.*, 2025, **105**, 44–53.
- 20 J. Wang, S. Tan, G. Zhang, Y. Jiang, Y. Yin, F. Xiong, Q. Li, D. Huang, Q. Zhang, L. Gu, Q. An and L. Mai, Fast and Stable Mg²⁺ Intercalation in a High Voltage NaV₂O₂(PO₄)₂/rGO Cathode Material for Magnesium-Ion Batteries, *Sci. China Mater.*, 2020, **63**(9), 1651–1662.
- 21 S. Li, Y. Sun, Y. Pang, S. Xia, T. Chen, H. Sun, S. Zheng and T. Yuan, Recent Developments of Layered Transition Metal Oxide Cathodes for Sodium-ion Batteries toward Desired High Performance, *Asia-Pac. J. Chem. Eng.*, 2022, **17**(4), e2762.
- 22 P. Panigrahi, S. B. Mishra, T. Hussain, B. R. K. Nanda and R. Ahuja, Density Functional Theory Studies of Si₂ BN Nanosheets as Anode Materials for Magnesium-Ion Batteries, *ACS Appl. Nano Mater.*, 2020, **3**(9), 9055–9063.
- 23 M. Mao, X. Ji, S. Hou, T. Gao, F. Wang, L. Chen, X. Fan, J. Chen, J. Ma and C. Wang, Tuning Anionic Chemistry To Improve Kinetics of Mg Intercalation, *Chem. Mater.*, 2019, **31**(9), 3183–3191.
- 24 Y. Zhang, Z. Yuan, L. Zhao, Y. Li, X. Qin, J. Li, W. Han and L. Wang, Review of Design Routines of MXene Materials for Magnesium-ion Energy Storage Device, *Small*, 2023, **19**(34), 2301815.
- 25 B. Zhou, H. Shi, R. Cao, X. Zhang and Z. Jiang, Theoretical Study on the Initial Stage of a Magnesium Battery Based on a V₂O₅ Cathode, *Phys. Chem. Chem. Phys.*, 2014, **16**(34), 18578–18585.
- 26 M. R. Lukatskaya, O. Mashtalir, C. E. Ren, Y. Dall'Agnese, P. Rozier, P. L. Taberna, M. Naguib, P. Simon, M. W. Barsoum and Y. Gogotsi, Cation Intercalation and High Volumetric Capacitance of Two-Dimensional Titanium Carbide, *Science*, 2013, **341**(6153), 1502–1505.
- 27 M. Naguib, M. W. Barsoum and Y. Gogotsi, Ten Years of Progress in the Synthesis and Development of MXenes, *Adv. Mater.*, 2021, **33**(39), 2103393.
- 28 D. Wang, Y. Gao, Y. Liu, D. Jin, Y. Gogotsi, X. Meng, F. Du, G. Chen and Y. Wei, First-Principles Calculations of Ti₂N and Ti₂NT₂ (T = O, F, OH) Monolayers as Potential Anode Materials for Lithium-Ion Batteries and Beyond, *J. Phys. Chem. C*, 2017, **121**(24), 13025–13034.
- 29 D. Er, J. Li, M. Naguib, Y. Gogotsi and V. B. Shenoy, Ti₃C₂ MXene as a High Capacity Electrode Material for Metal (Li, Na, K, Ca) Ion Batteries, *ACS Appl. Mater. Interfaces*, 2014, **6**(14), 11173–11179.
- 30 M. Naguib, J. Halim, J. Lu, K. M. Cook, L. Hultman, Y. Gogotsi and M. W. Barsoum, New Two-Dimensional Niobium and Vanadium Carbides as Promising Materials



- for Li-Ion Batteries, *J. Am. Chem. Soc.*, 2013, **135**(43), 15966–15969.
- 31 Z. Zhang, Z. Sun, S. Sun, J. Liu, J. Jiang, W. Shang and Y. Wen, MXene Modified Anode of Magnesium Battery to Improve the Problems of Voltage Lag and Irreversibility, *J. Alloys Compd.*, 2023, **960**, 170609.
- 32 J. Zhu, R. Shi, Y. Liu, Y. Zhu, J. Zhang, X. Hu and L. Li, 3D Interwoven MXene Networks Fabricated by the Assistance of Bacterial Celluloses as High-Performance Cathode Material for Rechargeable Magnesium Battery, *Appl. Surf. Sci.*, 2020, **528**, 146985.
- 33 R. Rajagopalan, Y. Tang, X. Ji, C. Jia and H. Wang, *Adv. Funct. Mater.*, 2020, 1909486.
- 34 G. Kresse and J. Hafner, Ab Initio Molecular Dynamics for Open-Shell Transition Metals, *Phys. Rev. B:Condens. Matter Mater. Phys.*, 1993, **48**(17), 13115–13118.
- 35 G. Kresse and J. Furthmüller, Efficient Iterative Schemes for Ab Initio Total-Energy Calculations Using a Plane-Wave Basis Set, *Phys. Rev. B:Condens. Matter Mater. Phys.*, 1996, **54**(16), 11169–11186.
- 36 P. E. Blöchl, Projector Augmented-Wave Method, *Phys. Rev. B:Condens. Matter Mater. Phys.*, 1994, **50**(24), 17953–17979.
- 37 G. Kresse and D. Joubert, From Ultrasoft Pseudopotentials to the Projector Augmented-Wave Method, *Phys. Rev. B:Condens. Matter Mater. Phys.*, 1999, **59**(3), 1758–1775.
- 38 J. P. Perdew and W. Yue, Accurate and Simple Density Functional for the Electronic Exchange Energy: Generalized Gradient Approximation, *Phys. Rev. B:Condens. Matter Mater. Phys.*, 1986, **33**(12), 8800–8802.
- 39 J. P. Perdew, K. Burke and M. Ernzerhof, Generalized Gradient Approximation Made Simple, *Phys. Rev. Lett.*, 1996, **77**(18), 3865–3868.
- 40 J. Luo, T. Fan, J. Zhang, P. Qiu, X. Shi and L. Chen, Automatic Identification of Slip Pathways in Ductile Inorganic Materials by Combining the Active Learning Strategy and NEB Method, *npj Comput. Mater.*, 2025, **11**(1), 41.
- 41 G. Henkelman, B. P. Uberuaga and H. Jónsson, A Climbing Image Nudged Elastic Band Method for Finding Saddle Points and Minimum Energy Paths, *J. Chem. Phys.*, 2000, **113**(22), 9901–9904.
- 42 G. Henkelman and H. Jónsson, Improved Tangent Estimate in the Nudged Elastic Band Method for Finding Minimum Energy Paths and Saddle Points, *J. Chem. Phys.*, 2000, **113**(22), 9978–9985.
- 43 C. Teng, Y. Wang and J. L. Bao, Physical Prior Mean Function-Driven Gaussian Processes Search for Minimum-Energy Reaction Paths with a Climbing-Image Nudged Elastic Band: A General Method for Gas-Phase, Interfacial, and Bulk-Phase Reactions, *J. Chem. Theory Comput.*, 2024, **20**(10), 4308–4324.
- 44 Q. Wang, J. Li, H. Jin, S. Xin and H. Gao, Prussian-blue Materials: Revealing New Opportunities for Rechargeable Batteries, *Infomat*, 2022, **4**(6), e12311.

